Progress In Electromagnetics Research M, Vol. 121, 13–26, 2023

Low-Frequency Magnetic Shielding of a Cavity Formed by Two Imperfectly Conducting Sheets: Effect of Sheet-to-Sheet Distance and Comparison with the Single-Sheet Configuration

Fubin Pang[1], Shi Chen[1], Jianfei Ji[1], Yiyi Jing[2], Sijia Liu[2], and Chongqing Jiao[2, *]

Abstract—In standard measurement methods such as NSA 94–106, the low-frequency magnetic shielding effectiveness of a shielding enclosure is tested using the near field of loop antenna. Under this near-field configuration, there is no analytical or closed-form solution for volumetric shielding like box/cavity except for planar shielding like a sheet of infinite extension. Exploring the correlation between volumetric shielding and planar shielding can provide simple prediction methods for volumetric shielding based on planar shielding. As a taste to this end, this article explores the difference between the shielding effectiveness of a double-sheet cavity and a single sheet under the NSA 94–106 standard. We derived the exact solution in integral form for electromagnetic fields inside the cavity and calculated the curves of shielding effectiveness on the frequency with different sheet material, thickness, and sheet-to-sheet distance. The results show that when the distance from the receiving antenna to the back sheet is greater than the diameter of the loop antenna, the results of a double-sheet cavity tend to be consistent with a single-sheet configuration. When the distance is less than the diameter, the difference between the two depends on material type and sheet thickness.

1. INTRODUCTION

Shielding of low-frequency magnetic fields is frequently needed in many practical applications involving high magnetic fields, such as wireless power transmission [1, 2], electric vehicles [3, 4], magnetic resonance imaging [5], pulse power systems [6], and spot welding guns [7]. The shielding effectiveness (SE) of a shielding structure depends not only on its geometry, size, and material but also on the selected field source and observation point [8, 9].

Here, we mainly focus on the geometry effect. Similar problems have been investigated to compare the shielding performance of conducting sheets, spherical shells, and cylindrical shells [9, 10]. The results quantitatively indicated the strong effect of geometry on shielding performance. However, the source is assumed to be a uniform magnetic field, which does not comply with the standard method for measuring SE, such as NSA 94–106 [11] and IEEE std-299 [12]. In the two standards, the magnetic field is generated by a current in a 0.3 m diameter loop antenna placed outside a shielding enclosure at a distance of 0.3 m, and the receive antenna also has a 0.3 m diameter loop placed inside the enclosure, as displayed in Fig. 1. The difference is that the two loops are coaxial for the former standard but coplanar for the latter standard.

Obviously, the magnetic field produced by such a source is nonuniform for most practical enclosures unless the size of the enclosure is very small, or it is very far from the loop antenna. We aim to investigate the effect of geometry in the case that the configuration of field source and receiver is in accordance

Received 26 April 2023, Accepted 27 October 2023, Scheduled 9 November 2023

* Corresponding author: Chongqing Jiao (cqjiao@ncepu.edu.cn).

[1] State Grid Jiangsu Electric Power Co., Ltd. Research Institute, Nanjing 211103, China. [2] State Key Laboratory of Alternate Electrical Power System with Renewable Energy Source, North China Electric Power University, Beijing 102206, China.

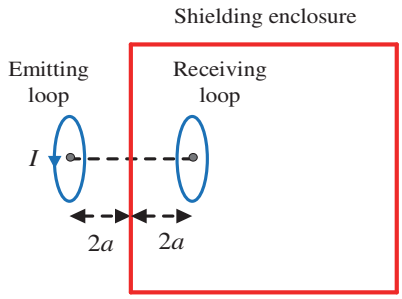

Figure 1. Sketch of magnetic shielding measurement of shielding enclosure in the standard method. The magnetic field is generated by a loop antenna outside the enclosure and is received by the other loop antenna inside the enclosure. Both the antennas have the same radius (a).

with the NSA 94–106 standard. The reason for selecting this standard rather than IEEE std-299 is that the coaxial configuration is easier to be solved than the coplanar configuration. The latter is left for future research. Although a 3D enclosure such as a rectangular box/cavity is closer to a practical situation, solving a 3D field problem is very difficult unless numerical techniques are used. To simplify the analysis of the problem, we adopt the special case of a cavity formed by two imperfectly conducting sheets, as indicated in Fig. 2, in which a is the loop radius, t the sheet thickness, and d the sheet-to-sheet distance. The distance from the emitting loop to the front sheet is $2a$, which is the same as the distance from the receiving loop to the sheet. Although this geometry is relatively simple, it has two advantages: 1) a closed-form expression can be derived; 2) the effect of sheet-to-sheet distance is contained. The conclusion for this simple geometry can provide a basic understanding of the effect of the size of the enclosure on SE. The conclusion may be even extended to 3D geometry to some degree. For example, when the distances from the receiving loop to the six walls of a rectangular cavity are all larger than some critical value, the SE will be determined primarily by the wall under test (the wall in the middle of the two loops). In other words, the SE of a rectangular cavity will be close to that of a single wall with infinite extension.

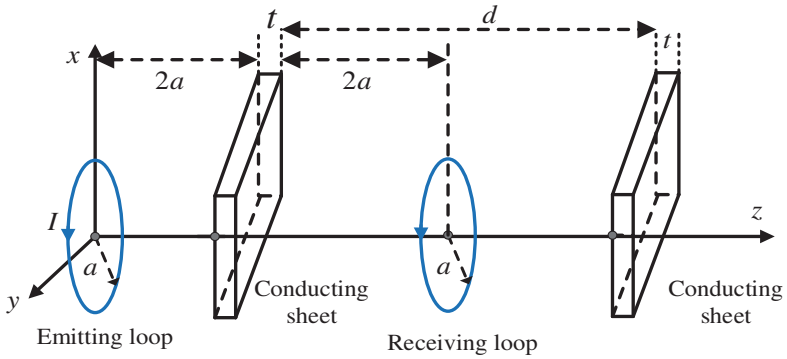

Figure 2. Configuration of magnetic shielding measurement of a cavity formed by two imperfectly conducting sheets. Wherein, a is the loop radius, t is the sheet thickness, d is the sheet-to-sheet distance, and $2a$ is the distance from emitting (receiving) loop to the sheet under test.

Intuitively, with the increase of the sheet-to-sheet distance d, the SE of the double-sheet configuration will tend to that of the corresponding single-sheet configuration with sheet 2 removed and sheet 1 remaining. To quantitatively address this concern, the single-sheet configuration shown in Fig. 3 is also solved for comparison with the double-sheet configuration. It should be noted, for single-sheet configuration, that its solution has been known and investigated widely [13–16].

The main contribution of this article includes 1) deriving the exact field distribution in integral from the shielding enclosure of a cavity formed by two imperfectly conducting sheets; 2) comparing the

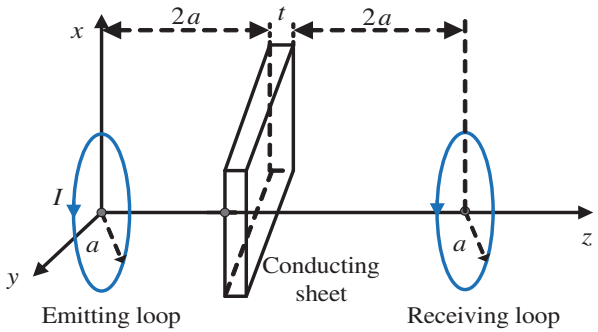

Figure 3. Configuration of magnetic shielding measurement of an imperfectly conducting sheet of infinite extension. Wherein, a is the loop radius, t is the sheet thickness, and $2a$ is the distance from emitting (receiving) loop to the sheet under test.

SE difference between the double-sheet configuration and single-sheet configuration and then showing the condition under which the two will be consistent. The rest of this article is organized as follows. In Section 2, the electromagnetic problem is described, and the exact solution in integral form is derived, based on the method of separation of variables in cylindrical coordinates. Also, the solutions for single-sheet configuration and free space are listed. In Section 3, some calculated SE-frequency curves are displayed with different shielding materials and thicknesses considered. Also, comparisons between double-sheet and single-sheet configurations are carried out. The conclusion on the effect of sheet-to-sheet distance is preliminarily extended to cylindrical cavities by finite element simulations. Finally, Section 4 concludes this article.

2. THEORETICAL MODEL

2.1. The Shielding Configuration

Figure 4 shows the geometrical configuration of the low-frequency magnetic field problem under consideration, where the magnetic field generated by the emitting loop is shielded by a cavity formed by two imperfectly conducting sheets. The emitting loop of radius a carrying a current I is placed with its axis coincident with the z-axis and with its center coincident with the origin. The current is time-harmonic with the angular frequency ω. A time-harmonic dependence $e^{j\omega t}$ is assumed and suppressed throughout. Sheet 1 has thickness t_1, electric permittivity ε_{s1}, magnetic permeability μ_{s1}, and bulk conductivity σ_{s1}. Sheet 2 has thickness t_2, electric permittivity ε_{s2}, magnetic permeability μ_{s2}, and bulk conductivity σ_{s2}. The distance from sheet 1 to sheet 2 is d, and the distance from sheet 1 to the emitting loop is b. Sheet 1 occupies the space region of $z_1 < z < z_2$, and sheet 2 occupies the space region of $z_3 < z < z_4$ wherein $z_1 = b$, $z_2 = b + t_1$, $z_3 = z_2 + d$, and $z_4 = z_3 + t_2$. The whole space is

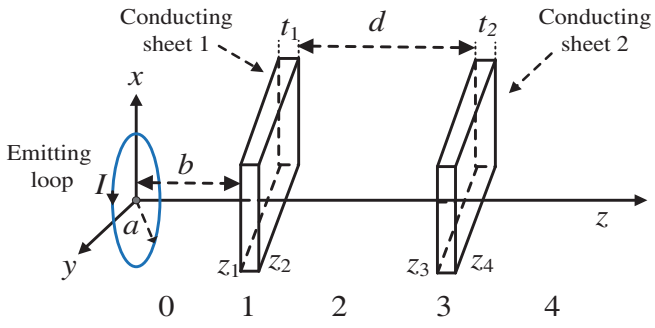

Figure 4. Low-frequency magnetic field generated by the loop antenna is shielded by a cavity formed by two imperfectly conducting sheets.

divided into five regions: region 0 ($0 < z < z_1$), region 1 ($z_1 < z < z_2$) region 2 ($z_2 < z < z_3$), region 3 ($z_3 < z < z_4$), and region 4 ($z > z_4$).

2.2. The Free-Space Fields

Since the above configuration is axisymmetric, a cylindrical coordinate (ρ, ϕ, z) is adopted. For this axisymmetric configuration, the exact electromagnetic field expressions in integral form can be obtained by solving the vector wave equation of the magnetic potential with the method of separation of variables in cylindrical coordinates. In fact, for a single-sheet configuration, its solution was obtained by Moser in 1967 [13]. The accuracy of the solutions was verified by comparing it with experimental results and finite element simulations [13–15].

The free space fields when the sheets are absent are listed as follows. These fields are named unshielded fields, which can be found in [13].

$$\mathbf{B}_{no}(\rho,z) = \frac{\mu_0 aI}{2}\mathbf{e}_\rho \int_0^\infty \lambda J_1(\lambda a) J_1(\lambda\rho) e^{-\tau_0 z} d\lambda + \frac{\mu_0 aI}{2}\mathbf{e}_z \int_0^\infty \frac{\lambda^2}{\tau_0} J_1(\lambda a) J_0(\lambda\rho) e^{-\tau_0 z} d\lambda \quad (1)$$

$$\mathbf{E}_{no}(\rho,z) = -\frac{j\omega\mu_0 aI}{2}\mathbf{e}_\phi \int_0^\infty \frac{\lambda}{\tau_0} J_1(\lambda a) J_1(\lambda\rho) e^{-\tau_0|z|} d\lambda \quad (2)$$

$$\tau_0 = \sqrt{\lambda^2 - k_0^2} \quad (3)$$

$$k_0 = \omega\sqrt{\mu_0\varepsilon_0} \quad (4)$$

where μ_0 is the free space magnetic permeability; ε_0 is the free space permittivity; $j = (-1)^{1/2}$; J_1 is the Bessel function of order one; k_0 is the free space wavenumber; λ is the transverse wavenumber; and τ_0 is the longitudinal propagation constant.

2.3. The Fields of Double-Sheet Configuration

Moser's method is also applicable to multi-sheet configuration by modeling each sheet (layer) as an individual field domain and combining them by the boundary conditions. Here, we provide the main procedure to derive the solution, following Moser's method. For the double-sheet configuration shown in Fig. 2, the fields in the nth region can be expressed as

$$\begin{aligned}\mathbf{B}_n(\rho,z) = {} & \frac{\mu_0 aI}{2}\mathbf{e}_\rho \int_0^\infty \lambda J_1(\lambda a) J_1(\lambda\rho)\left(D_n e^{-\tau_n z} - C_n e^{\tau_n z}\right) d\lambda \\ & + \frac{\mu_0 aI}{2}\mathbf{e}_z \int_0^\infty \frac{\lambda^2}{\tau_n} J_1(\lambda a) J_0(\lambda\rho)\left(D_n e^{-\tau_n z} + C_n e^{\tau_n z}\right) d\lambda \end{aligned} \quad (5)$$

$$\mathbf{E}_n(\rho,z) = -\frac{j\omega\mu_0 aI}{2}\mathbf{e}_\phi \int_0^\infty \frac{\lambda}{\tau_n} J_1(\lambda a) J_1(\lambda\rho)\left(D_n e^{-\tau_n z} + C_n e^{\tau_n z}\right) d\lambda \quad (6)$$

$$\tau_n = \sqrt{\lambda^2 - k_n^2} \quad (7)$$

$$k_n^2 = \omega^2\mu_n\left(\varepsilon_n - j\frac{\sigma_n}{\omega}\right) \quad (8)$$

where $n = 0$, 1, 2, 3, and 4 corresponding to regions 0, 1, 2, 3, and 4, respectively, as displayed in Fig. 4. The coefficients D_n and C_n are responsible for the forward ($+z$) and backward ($-z$) wave amplitudes, respectively. ε_n, μ_n, and σ_n denote the permittivity, permeability, and conductivity of the nth region, respectively. For region 0, the forward wave should be identical to the free-space fields. Hence,

$$D_0 = 1 \quad (9)$$

For Region 4, there should be no backward wave, so

$$C_4 = 0 \quad (10)$$

By applying the continuation conditions of tangential components of E and H fields at the four boundary surfaces ($z = z_1$, z_2, z_3, and z_4), the following relationship between the coefficients can be

obtained

$$\begin{bmatrix} D_{n+1} \\ C_{n+1} \end{bmatrix} = \begin{bmatrix} \frac{\mu_n}{2\mu_{n+1}} e^{(\tau_{n+1}-\tau_n)z_{n+1}} \left(\frac{\tau_{n+1}}{\tau_n} + \frac{\mu_{n+1}}{\mu_n} \right) & \frac{\mu_n}{2\mu_{n+1}} e^{(\tau_n+\tau_{n+1})z_{n+1}} \left(\frac{\tau_{n+1}}{\tau_n} - \frac{\mu_{n+1}}{\mu_n} \right) \\ \frac{\mu_n}{2\mu_{n+1}} e^{-(\tau_n+\tau_{n+1})z_{n+1}} \left(\frac{\tau_{n+1}}{\tau_n} - \frac{\mu_{n+1}}{\mu_n} \right) & \frac{\mu_n}{2\mu_{n+1}} e^{-(\tau_{n+1}-\tau_n)z_{n+1}} \left(\frac{\tau_{n+1}}{\tau_n} + \frac{\mu_{n+1}}{\mu_n} \right) \end{bmatrix} \begin{bmatrix} D_n \\ C_n \end{bmatrix} \tag{11}$$

Combining Eqs. (9)–(11), all the coefficients D_n and C_n can be determined.

In the following, we focus on the special case where both conducting sheets are of the same material and thickness, that is $\mu_1 = \mu_2 = \mu$, $\varepsilon_1 = \varepsilon_2 = \varepsilon$, $\sigma_1 = \sigma_2 = \sigma$, $t_1 = t_2 = t$. Also, since our aim is to analyze the shielding effectiveness of the cavity formed by the two imperfectly conducting sheets, the fields within Region 2 are primarily concerned, and hence D_2 and C_2 are listed here,

$$D_2 = \frac{4K^2\mu_r^2 \left[e^{(\tau+\tau_0)t} \left(2 + \frac{\tau_0\mu}{\mu_0\tau} + \frac{\mu_0\tau}{\tau_0\mu} \right) + e^{-(\tau-\tau_0)t} \left(2 - \frac{\tau_0\mu}{\mu_0\tau} - \frac{\mu_0\tau}{\tau_0\mu} \right) \right]}{(K+\mu_r)^2 (K-\mu_r)^2 \left\{ (e^{-2\tau_0 d}-1) \left[2 - e^{-2\tau t} - e^{2\tau t} \right] + e^{-2\tau t} \left[\frac{(K-\mu_r)^2}{(K+\mu_r)^2} - 1 \right] + e^{2\tau t} \left[\frac{(K+\mu_r)^2}{(K-\mu_r)^2} - 1 \right] \right\}} \tag{12}$$

$$C_2 = \frac{-4e^{2\tau_0 t} K^2\mu_r^2 \left[e^{\tau t} e^{-\tau_0(z_4+z_3)} \left(\frac{\tau}{\tau_0}\frac{\mu_0}{\mu} - \frac{\mu}{\mu_0}\frac{\tau_0}{\tau} \right) + e^{-\tau t} e^{-\tau_0(z_4+z_3)} \left(\frac{\mu}{\mu_0}\frac{\tau_0}{\tau} - \frac{\tau}{\tau_0}\frac{\mu_0}{\mu} \right) \right]}{(K+\mu_r)^2 (K-\mu_r)^2 \left\{ (e^{-2\tau_0 d}-1) \left[2 - e^{-2\tau t} - e^{2\tau t} \right] + e^{-2\tau t} \left[\frac{(K-\mu_r)^2}{(K+\mu_r)^2} - 1 \right] + e^{2\tau t} \left[\frac{(K+\mu_r)^2}{(K-\mu_r)^2} - 1 \right] \right\}} \tag{13}$$

$$K = \tau/\tau_0, \mu_r = \mu/\mu_0 \tag{14}$$

$$\tau = \sqrt{\lambda^2 - k^2} \tag{15}$$

$$k^2 = \omega^2\mu \left(\varepsilon - j\frac{\sigma}{\omega} \right) \tag{16}$$

Substituting Eqs. (12)–(13) into Eqs. (5)–(6), the solution of the fields within the cavity is obtained.

Especially, the E field solution in Region 2 is listed here, since it will be used in the following calculation.

$$E_2(\rho, z) = -4j\omega\mu_0 aI \int_0^\infty \frac{\lambda J_1(\lambda a) J_1(\lambda\rho) K^2\mu_r^2}{\tau_0} \frac{2e^{-\tau_0(z-t)} \left[\cosh(\tau t) + \frac{1}{2} \left(\frac{\mu_r}{K} + \frac{K}{\mu_r} \right) \sinh(\tau t) \right] - e^{-\tau_0(z_4+z_3-z-2t)} \left(\frac{K}{\mu_r} - \frac{\mu_r}{K} \right) \sinh(\tau t)}{(K^2-\mu_r^2)^2 \left\{ (e^{-2\tau_0 d}-1) \left[2 - \cosh(2\tau t) \right] + e^{-2\tau t} \left[\frac{(K-\mu_r)^2}{(K+\mu_r)^2} - 1 \right] + e^{2\tau t} \left[\frac{(K+\mu_r)^2}{(K-\mu_r)^2} - 1 \right] \right\}} d\lambda \tag{17}$$

It should be noted that by using $t = 0$, the above results can be simplified into free-space fields, as displayed in Eqs. (1)–(2).

2.4. The Fields of Single-Sheet Configuration

A single-sheet configuration can be considered as the special case of a double-sheet configuration with the sheet-to-sheet distance d tending to infinity. In this special case, we can use $e^{-2\tau_0 d} \to 0$, $e^{-\tau_0(z_4+z_3)} \to 0$ to simplify Eqs. (12)–(13), then the fields in Region 2 can be written as

$$\mathbf{B}_s = 2\mu aI\mathbf{e}_\rho \int_0^\infty \frac{C\lambda\tau}{\tau_0} J_1(\lambda a) J_1(\lambda\rho) e^{-\tau_0 z - t(\tau-\tau_0)} d\lambda + 2\mu aI\mathbf{e}_z \int_0^\infty \frac{C\lambda^2\tau}{\tau_0^2} J_1(\lambda a) J_0(\lambda\rho) e^{-\tau_0 z - t(\tau-\tau_0)} d\lambda \tag{18}$$

$$\mathbf{E}_s = -2j\omega\mu a I \mathbf{e}_\phi \int_0^\infty \frac{C\lambda\tau}{\tau_0^2} J_1(\lambda a) J_1(\lambda\rho_p) e^{-\tau t} e^{-\tau_0(z-t)} d\lambda \tag{19}$$

$$C = \frac{1}{(K+\mu_r)^2 - e^{-2\tau t}(K-\mu_r)^2} \tag{20}$$

Not surprisingly, they are identical to the existing results for single-sheet configuration [13].

2.5. The Shielding Effectiveness

The shielding effectiveness (SE) is defined as

$$SE = 20\log_{10}|V_{without}/V_{with}| \tag{21}$$

where $V_{without}$ denotes the open-circuit voltage measured by the receiving loop when the sheets are absent, and V_{with} represents the voltage measured by the receiving loop when the sheet is present. Thanks to the axisymmetric distribution, $V_{without}$ and V_{with} are directly related to the free-space E field and shielded E field in region 2, respectively, like

$$V_{without} = 2\pi a E_{no}(a, z_p) \tag{22}$$

$$V_{with} = 2\pi a E_2(a, z_p) \tag{23}$$

where a is the aforementioned radius of the receiving loop, and z_p denotes the distance from the receiving loop to the emitting loop. For single-sheet configuration, E_2 in Eq. (22) should be replaced with E_s.

Due to the presence of $e^{-\tau}0^z$ in Eqs. (2), (17), and (19), the integrand becomes vanishingly small for large λ, and hence restricting the integration to a finite range of 0 ¡ $\lambda < \lambda_m$ does not significantly alter the value of the integral. According to [17, 18], $\lambda_m = 10/z$ is satisfactory, where z denotes the distance between the field point and the plane on which the loop lies.

3. RESULTS AND DISCUSSIONS

In accordance with the standard NSA 94–106 [11], we let $a = 0.15\,\text{m}$ and $b = 0.3\,\text{m}$. The frequency range is limited between 10 Hz and 1 MHz. For lower frequencies, the SE usually is the same as that at 10 Hz. For higher frequencies, the SE of the metallic sheet is very high so that the sheet can be considered as a perfectly electric conductor, and the only field penetration path is usually the apertures/seams on the sheet [19–21] or the edge effect for sheets with finite size [15, 22].

3.1. Comparisons with Finite Element Simulations

When the sheet is made of aluminum ($u_r = 1$, $\sigma = 3.78 \times 10^7\,\text{S/m}$, $t = 0.5\,\text{mm}$), the dependence of SE on frequency is plotted in Fig. 5 for two sheet-to-sheet distances: 0.32 m and 0.6 m. The solid curves result from the derived integral formula; the dashed curves result from finite element simulations carried by a two-dimension axisymmetric model built in the commercial COMSOL software [23]. The two are in good agreement if the frequency is lower than 200 kHz. Beyond this range, the finite element method (FEM) results are affected by the edge effect, since the sheet has finite size (1.2 m in radius) in the FEM model. Similar phenomena have been observed in [15, 22].

3.2. More Results for Aluminum Sheet

Here, two other thicknesses of aluminum sheet are selected: $t = 0.1\,\text{mm}$ for Fig. 6 and $t = 1\,\text{mm}$ for Fig. 7. For each thickness, four SE curves are plotted. Among them, one curve is for single-sheet configuration, and the other three curves are for double-sheet configurations ($d = 0.32\,\text{m}$, $0.4\,\text{m}$, and $0.6\,\text{m}$, respectively). Especially, we add the results for SE differences, which are obtained by subtracting the SE of single-sheet configuration from that of double-sheet configurations. From Figs. 6(b) and 7(b), we can see that all the SE differences are firstly enhanced with the frequency increase and then tend to unchanged above some critical frequency. The reason is that for higher frequencies the sheet will tend to behave like a perfect electric conductor. The critical frequency is about 3 kHz for $t = 0.1\,\text{mm}$ and about 1 kHz for $t = 1\,\text{mm}$. In the stable stage, the SE differences are about 13 dB, 3 dB, and 0 dB

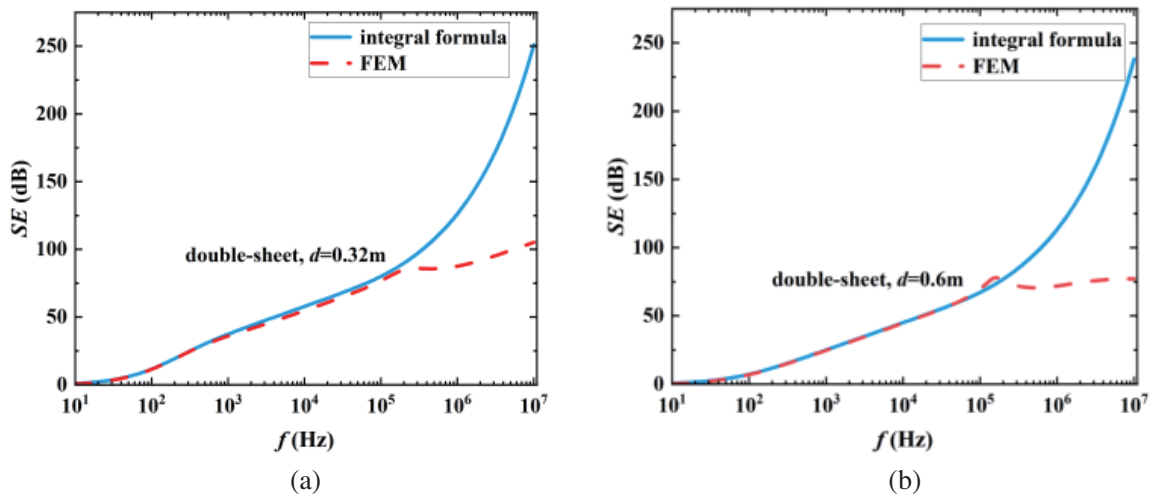

Figure 5. SE of the double-sheet cavity made of aluminum: the solid curves result from the integral formula; the dashed curves result from finite element simulations. (a) The sheet-to-sheet distance $d = 0.32\,\text{m}$. (b) The sheet-to-sheet distance $d = 0.6\,\text{m}$.

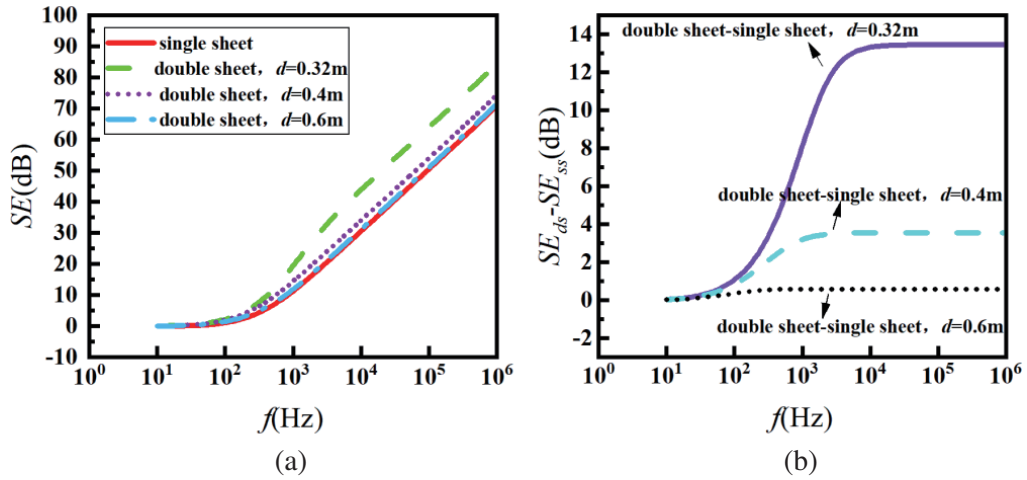

Figure 6. The SE of 0.1 mm aluminum sheet in single-sheet configuration and double-sheet configurations with $d = 0.32\,\text{m}$, $0.4\,\text{m}$, and $0.6\,\text{m}$ (a); the differences of each of double-sheet configurations relative to the single-sheet configuration (b).

for $d = 0.32\,\text{m}$, $0.4\,\text{m}$, and $0.6\,\text{m}$, respectively. On the other hand, the SE differences increase with the sheet-to-sheet distance d declining. The SE in the case of $d = 0.6\,\text{mm}$ is approximately equal to that of the single-sheet configuration. When $d = 0.6\,\text{m}$, the distances from the receiving loop to both the front and back sheets are both equal to the loop diameter. Hence, it is implied that the SE of a double-sheet configuration is close to that of a single-sheet configuration when the spacing from receiving loop to all the sheets is larger than the loop diameter. Of course, the above discussions are not suitable when the frequency is so high that the resonance effect within the cavity will occur. One rough estimate for the lowest resonance frequency is that the corresponding wavelength is about two times of the sheet-to-sheet distance d. For $d = 0.6\,\text{m}$, the resonance frequency is about 250 MHz. Conservatively, when the applied frequency is lower than one-tenth of the resonance frequency, the resonance effect can be safely neglected. In this sense, for the present concern for frequencies below 1 MHz, the maximum value of d is about 15 m ($= 250\,\text{MHz}/10/1\,\text{MHz} \times 0.6\,\text{m}$).

3.3. Results for Steel Sheet

Here, the steel sheet is made of commercial 1010 low-carbon steel with $\mu_r = 200$ and $\sigma = 9\times10^6$ S/m [8]. Two thicknesses are selected: $t = 0.5$ mm for Fig. 8 and $t = 1$ mm for Fig. 9. It is noted that, compared with the aluminum cases, the steel cases show a similar tendency in terms of SE difference for frequencies larger than 100 Hz. For such a frequency range, eddy current cancellation is the primary magnetic shielding mechanism. In contrast, for frequencies below 100 Hz, magnetic flux shunting is dominant, and hence the SE differences display the opposite tendency. That is, the larger the distance d is, the higher the corresponding SE is. This point will be further indicated in the following part for purely magnetic material.

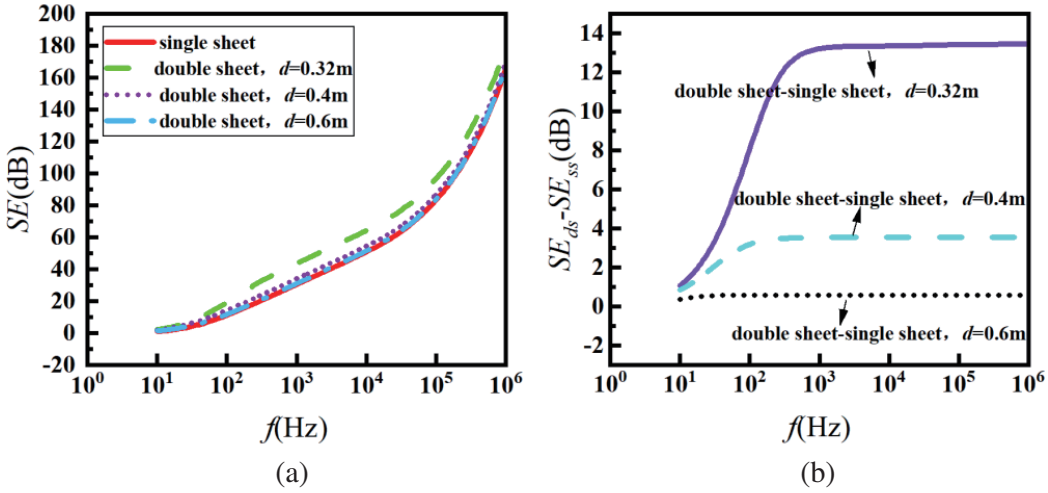

Figure 7. The SE of 1 mm aluminum sheet in single-sheet configuration and double-sheet configurations with $d = 0.32$ m, 0.4 m, and 0.6 m (a); the differences of each of double-sheet configurations relative to the single-sheet configuration (b).

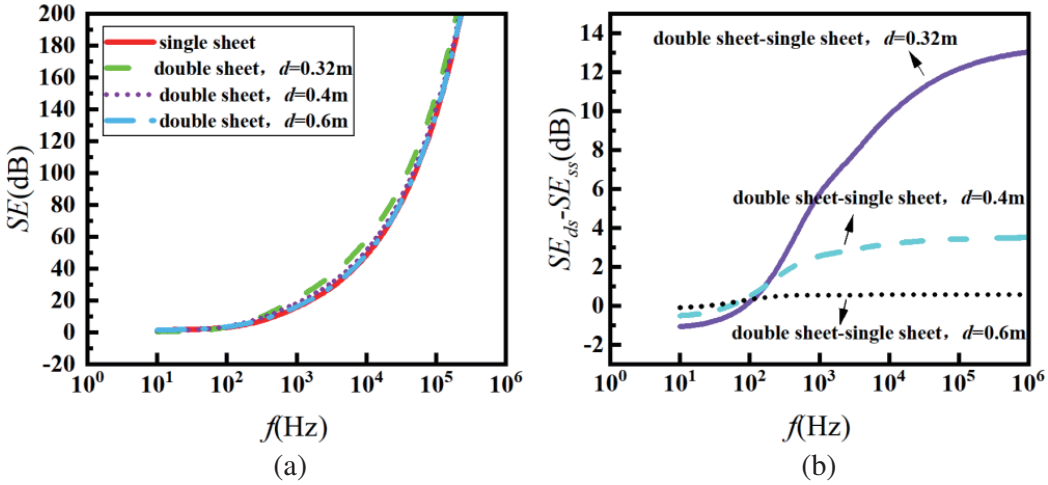

Figure 8. The SE of 0.5 mm steel sheet in single-sheet configuration and double-sheet configurations with $d = 0.32$ m, 0.4 m, and 0.6 m (a); the differences of each of double-sheet configurations relative to the single-sheet configuration (b).

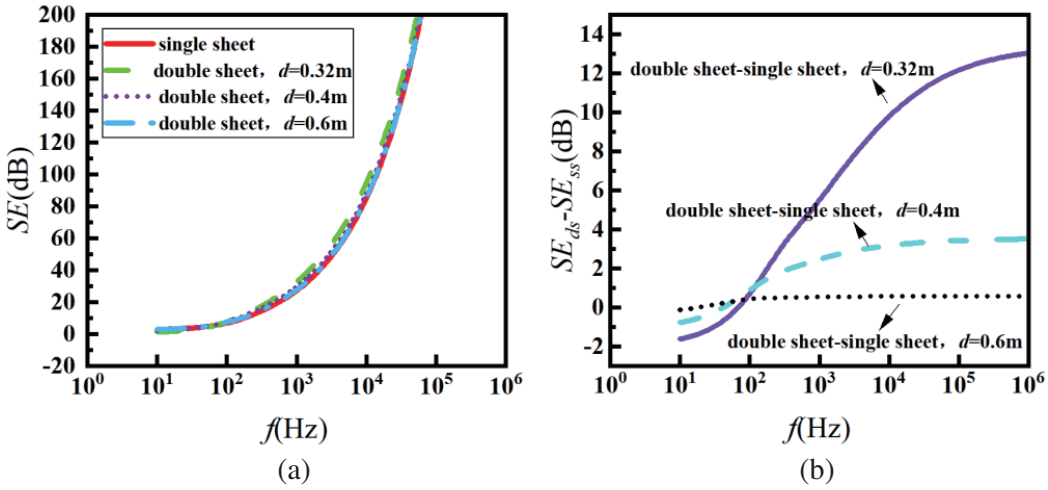

Figure 9. The SE of 1 mm steel sheet in single-sheet configuration and double-sheet configurations with $d = 0.32$ m, 0.4 m, and 0.6 m (a); the differences of each of double-sheet configurations relative to the single-sheet configuration (b).

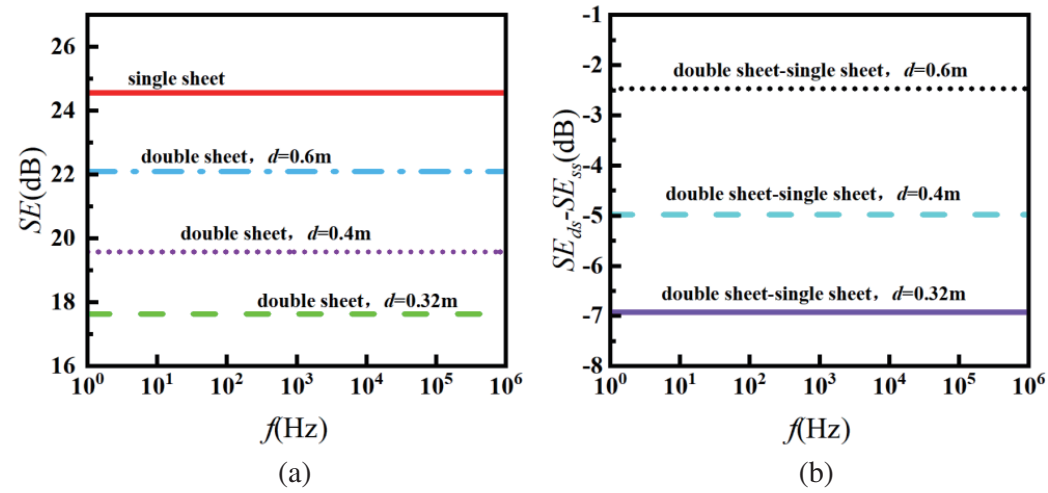

Figure 10. The SE of 1 mm magnetic sheet in single-sheet configuration and double-sheet configurations with $d = 0.32$ m, 0.4 m, and 0.6 m (a); the differences of each of double-sheet configurations relative to the single-sheet configuration (b).

3.4. Results for Magnetic Sheet

Here, a magnetic sheet means that it is magnetic but not conductive. It has a relative permeability of 10^4 and a thickness of 1 mm. In Fig. 10(a), the SE of the magnetic sheet is plotted as the function of frequency for single-sheet configuration and double-sheet configurations with $d = 0.32$ m, 0.4 m, and 0.6 m, respectively. As expected, the SE is not frequency-dependent. The corresponding difference of each double-sheet configuration relative to the single-sheet configuration is indicated in Fig. 10(b), which shows that for magnetic material the double-sheet configurations have lower SE than the single-sheet configuration. Moreover, the difference becomes larger with the distance d decreasing. This tendency is opposite to that observed in the case of aluminum sheets but is similar to that observed in the case of steel sheets with frequencies below 100 Hz.

3.5. Results for a Cylindrical Box

Through the above discussions, we guess that for a three-dimension enclosure like a box, its SE based on NSA 94–106 measurement method is approximately equal to that of the corresponding single-sheet configuration, if only the distances from the receiving loop to all the inner walls of the box all are larger than the diameter of the loop. To validate this judgment, a cylindrical box with all its walls having a 0.3 m distance to the receiving loop is considered. The box is made of aluminum and has a thickness of 0.5 mm, a radius of 0.45 m, and a height of 0.6 m, as shown in Fig. 11.

The SE of this box is compared with that of the corresponding single-sheet configuration, as displayed in Fig. 12. Good agreement is observed for the whole considered frequency range. Of course, the resonance effect is not involved since the highest frequency is far lower than the lowest resonance frequency (above 100 MHz).

To consider the effect of the position of the receiving loop, the distance from the receiving loop to the front wall, d_i, is changed, as shown in Fig. 13. The SE results for $d_i = 0.3$ m, 0.4 m, and 0.5 m are

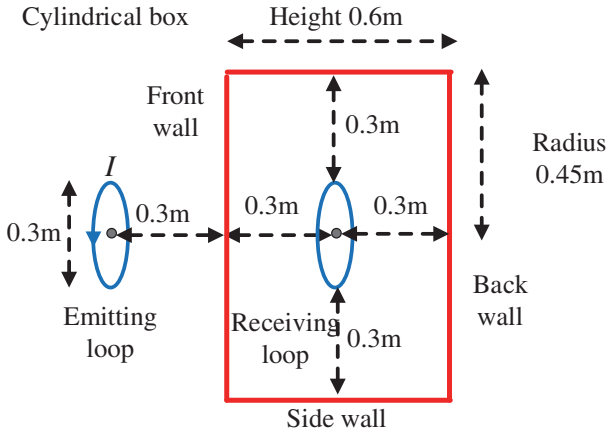

Figure 11. The shielding problem of a cylindrical box made of aluminum. The box has a thickness of 0.5 mm, a radius of 0.45 m, and a height of 0.6 m.

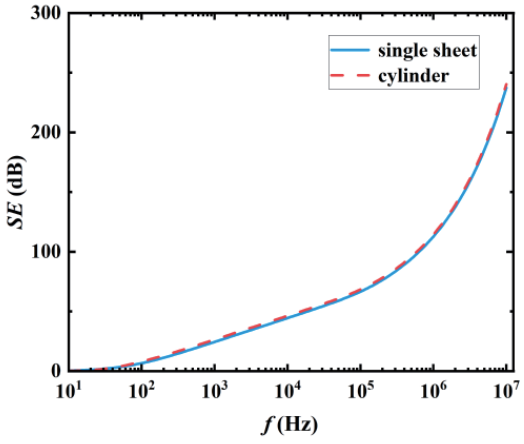

Figure 12. Comparison of the SE of the cylindrical box in Fig. 11 with that of the corresponding single-sheet configuration.

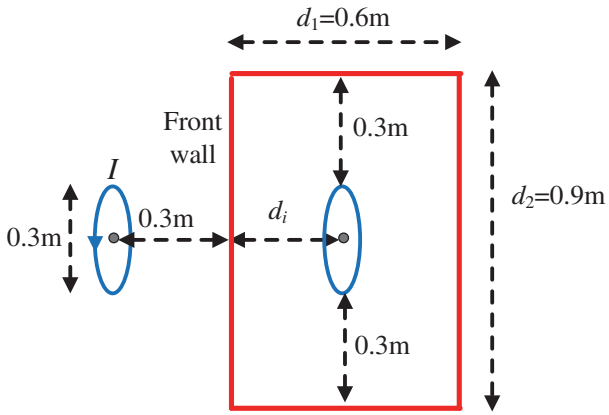

Figure 13. The shielding problem of a cylindrical box made of aluminum. The box has a thickness of 0.5 mm, a diameter of 0.9 m, and a height of 0.6 m. The receiving loop has a distance of d_i to the left wall.

shown in Fig. 14, in which the size of box is fixed with the height of 0.6 m and diameter of 0.9 m. The results show that the agreement between the box and the single-sheet configuration deteriorates with the receiving loop closer to the back wall. The difference is about 7 dB for $d_i = 0.5$ m (or the receiving loop to back wall distance is 0.1 m). The difference tends to be stable with frequency increasing once the frequency is higher than 400 Hz. The underlying physical mechanism is listed as follows. The eddy current induced on the conducting sheets/walls is responsible for the magnetic field reduction within the cavity/box. The maximum eddy current occurs on the wall/sheet between the two loops. As a result, the SE is primarily determined by this wall/sheet. For other walls, they will have obvious influence on the SE only when they are so close to the receiving loop that the magnetic field around the receiving loop is perturbed obviously by the walls.

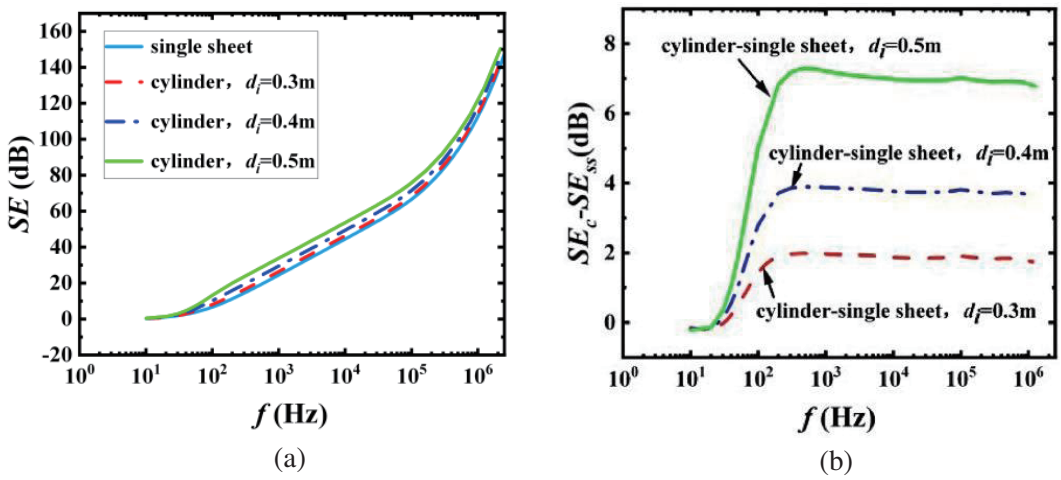

Figure 14. Comparison of the SE of the cylindrical box in Fig. 13 with that of the corresponding single-sheet configuration. (a) The dependence of the SE on frequency. (b) The SE differences of cylindrical box configurations relative to the single-sheet configuration.

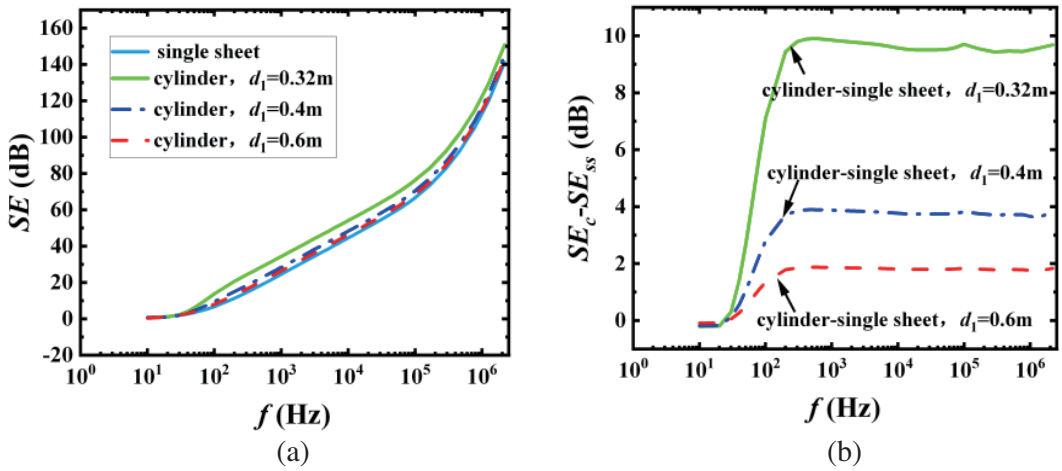

Figure 15. Comparison of the SE of the cylindrical box in Fig. 11 with that of the corresponding single-sheet configuration. Wherein, the diameter of the box is fixed at 0.9 m, but the height d_1 have different values: 0.32 m, 0.4 m and 0.6 m. (a) The dependence of the SE on frequency. (b) The SE differences of box configurations relative to single-sheet configuration.

The effect of the height of the box (d_1) is investigated in Fig. 15, in which the diameter of the box is 0.9 m, and the receiving loop to the front wall distance is 0.3 m. The following values of d_1 are considered: $d_1 = 0.32$ m, 0.4 m, and 0.6 m. As shown in Fig. 15(b), the difference between the two configurations increases with d_1 decrease. The difference is about 10 dB for $d_1 = 0.32$ m for frequencies above 300 Hz. The effect of the diameter of the box (d_2) is investigated in Fig. 16, in which the height of the box is 0.6 m, and the receiving loop to the front wall distance is 0.3 m. The following values of d_2 are considered: $d_1 = 0.32$ m, 0.5 m, and 0.9 m. As shown in Fig. 16(b), the difference between the two configurations increases with d_2 decrease. The difference is about 4 dB for $d_2 = 0.32$ m for frequencies above 300 Hz.

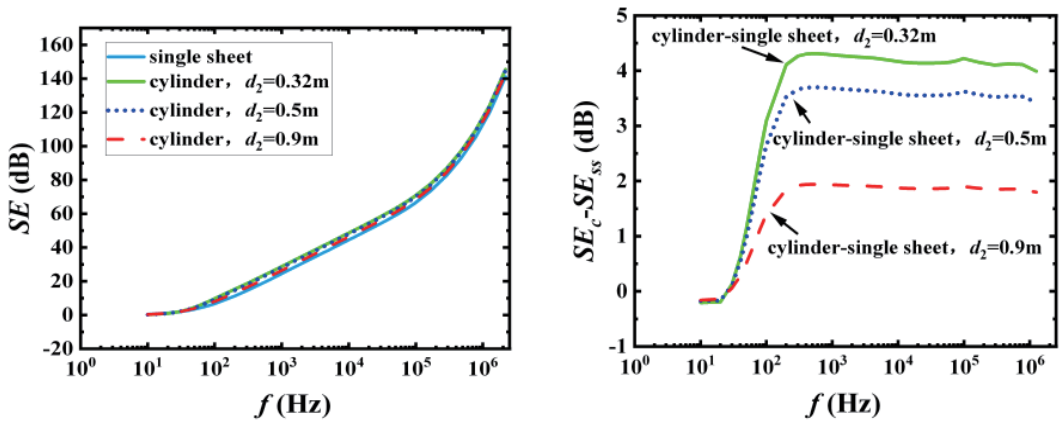

(a) (b)

Figure 16. Comparison of the SE of the cylindrical box in Fig. 11 with that of the corresponding single-sheet configuration. Wherein, the height of the box is fixed at 0.6 m, but the diameter d_2 has different values: 0.32 m, 0.5 m and 0.9 m. (a) The dependence of the SE on frequency. (b) The SE differences of box configurations relative to single-sheet configuration.

4. CONCLUSIONS

The exact solutions in integral form have been derived for electromagnetic fields within a cavity formed by two imperfectly conducting sheets of infinite extension when the two sheets are excited by a circular loop antenna placed with its axis perpendicular to the sheets. The shielding effectiveness of the double-sheet cavity is calculated under the NSA 94–106 standard when the two sheets are of the same material and thickness. The results are validated by comparisons with finite element simulations. The results show that the double-sheet configuration has similar shielding effectiveness to the single-sheet configuration when the distance from the receiving loop to the back sheet is also increased to the loop radius. When the distance is smaller than the radius, the SE of the double-sheet configuration is higher/lower than that of the single-sheet configuration for conducting/magnetic sheets (eddy current cancellation/magnetic shielding mechanism). In contrast, for frequencies below 100 Hz, magnetic flux shunting is dominant, and hence the SE differences display the opposite tendency. Further finite element simulations for a cylindrical box show that the SE is approximately equal to that of a corresponding single-sheet configuration if only the distances from the receiving loop to all the walls of the shielding box are larger than the loop antenna. Finally, it should be noted that the present discussions are limited to low-frequency cases that the cavity resonance effect can be neglected. For higher frequencies where the resonance effect is evident, the conclusions will no longer be feasible. Finally, it is noted that the present conclusion is limited to the case specified by the NSA 94–106 standard. For other configurations having different sizes of box, different positions of loop, and different sizes of loop, more calculations and parameter analysis are needed in the future.

ACKNOWLEDGMENT

This project is supported by State Grid Jiangsu Electric Power Co., Ltd., "Research on transmission characteristics and anti-interference measures for electromagnetic interference in power substation" (grant No. J2022121).

REFERENCES

1. Zhou, Y., L. Zhang, and S. Xiu, "Design and analysis of platform shielding for wireless charging tram," *IEEE Access*, Vol. 7, 129443–129451, 2019.
2. Lee, S., D. H. Kim, Y. Cho, et al., "Low leakage electromagnetic field level and high efficiency using a novel hybrid loop-array design for wireless high power transfer system," *IEEE Trans. Ind. Electron.*, Vol. 66, No. 6, 4356–4367, Jul. 2018.
3. Mohammad, M., E. T. Wodajo, S. Choi, et al., "Modeling and design of passive shield to limit EMF emission and to minimize shield loss in unipolar wireless charging system for EV," *IEEE Transactions on Power Electronics*, Vol. 34, No. 12, 12235–12245, 2019.
4. Mou, W. and M. Lu, "Research on shielding and electromagnetic exposure safety of an electric vehicle wireless charging coil," *Progress In Electromagnetics Research C*, Vol. 117, 55–72, 2021.
5. Kellogg, J., "Navigating the selection of magnetic resonance imaging shielding systems," *IEEE Transactions on Electromagnetic Compatibility*, Vol. 3, No. 1, 43–46, 2021.
6. Collier, L., et al., "Magnetic field diffusion in medium-walled conductors," *IEEE Transactions on Plasma Science*, Vol. 47 No. 1, 1024–1031, 2019.
7. Giaccone, L., V. Cirimele, and A. Canova "Mitigation solutions for the magnetic field produced by MFDC spot welding guns," *IEEE Transactions on Electromagnetic Compatibility*, Vol. 62, No. 1, 83–92, 2020.
8. Celozzi, S., R. Araneo, and G. Lovat, *Electromagnetic Shielding: Theory and Applications*, 2nd Edition, Wiley, Hoboken, NJ, USA, 2023.
9. Tesche, F. M., M. V. Ianoz, and T. Karlsson, *EMC Analysis Methods and Computational Models*, Wiley-Interscience Press, New York, 1996.
10. Lee, K. S. H., and G. Bedrosian, "Diffusive electromagnetic penetration into metallic enclosures," *IEEE Trans. Antennas Propagat.*, Vol. 27, No. 2, 194–198, 1979.
11. Specification for Shielded Enclosures, *Specification NSA*, 94–106, 1994.
12. IEEE Standard Method for Measuring the Effectiveness of Electromagnetic Shielding Enclosures, *IEEE Standard 299-2006*, 2007.
13. Moser, J. R., "Low-frequency shielding of a circular loop electromagnetic field source," *IEEE Trans. Electromagn. Compat.*, Vol. 9, No. 1, 6–18, 1967.
14. Qin, D. and C. Jiao, "Low-frequency magnetic shielding of planar screens: effects of loop radius and loop-to-loop distance," *IEEE Transactions on Electromagnetic Compatibility*, Vol. 64, No. 2, 367–377, 2021.
15. Andrieu, G., J. Panh, A. Reineix, et al., "Homogenization of composite panels from a near-field magnetic shielding effectiveness measurement," *IEEE Transactions on Electromagnetic Compatibility*, Vol. 54, No. 3, 700–703, Jun. 2012.
16. Lovat, G., P. Burghignoli, R. Araneo, and S. Celozzi, "Magnetic shielding of planar metallic screens: A new analytical closed-form solution," *IEEE Transactions on Electromagnetic Compatibility*, Vol. 62, No. 5, 1884–1888, Oct. 2020.
17. Ryan, C. M., "Computer expression for predicting shielding effectiveness for the low-frequency plane shield case," *IEEE Transactions on Electromagnetic Compatibility*, Vol. 9, No. 2, 83–94, 1967.
18. Jiao, C., F. Ning, X. Yang, et al., "Low-frequency magnetic shielding of planar shields: A unified wave impedance formula for the transmission line analogy," *IEEE Transactions on Electromagnetic Compatibility*, Vol. 63, No. 4, 1046–1057, 2021.

19. Matsuzawa, S., T. Kojima, K. Mizuno, et al., "Electromagnetic simulation of low-frequency magnetic shielding of a welded steel plate," *IEEE Transactions on Electromagnetic Compatibility*, Vol. 63, No. 6, 1896–1903, 2021.
20. Zhang, Z., X. Yang, C. Jiao, et al., "Analytical model for low-frequency magnetic field penetration through a circular aperture on a perfect electric conductor plate," *IEEE Transactions on Electromagnetic Compatibility*, Vol. 63, No. 5, 2599–1604, 2021.
21. Sun, Z., W. Dong, D. Y. Qin, et al., "Approximate simulation of low-frequency magnetic shielding of a rectangular shielding box with all walls perforated periodical holes," *Progress In Electromagnetics Research Letters*, Vol. 117, 55–72, 2021.
22. Lovat, G., P. Burghignoli, R. Araneo, et al., "Shielding of an imperfect metallic thin circular disk: Exact and low-frequency analytical solution," *Progress In Electromagnetics Research*, Vol. 167, 1–10, Jan. 2020.
23. Comsol software, [Online] Available: https://www.comsol.asia/comsol-multiphysics.